SpaceOps-2025, ID #517

Multiphysics Topology Optimization for Reaction Wheel Devices

Ricky Gill [a], Ahmad Z. Naser [b], Philip Ferguson [a*]

[a] *Space Technology and Advanced Research Lab, Department of Mechanical Engineering, University of Manitoba, Winnipeg, MB R3T5V6*
[b] *Department of Mechanical Engineering, University of Manitoba, Winnipeg, MB R3T5V6*
* Corresponding Author

Abstract

By sharing a launch vehicle with multiple payloads, small satellites reduce the frequency of individual launches, lowering costs and minimizing the environmental impact of rocket emissions. However, spacecraft performance is often constrained by limited pointing accuracy and control authority, as mass, volume, and power restrictions prevent the integration of reaction wheels with sufficient momentum storage and torque. A unified approach that concurrently addresses electromagnetic and structural design objectives in reaction wheel development remains largely unexplored but holds the potential to enhance small satellite agility and efficiency. This research presents a multiphysics-compatible optimization framework for designing compact, high-performance reaction wheels. The developed algorithm integrates NSGA-II with the A-Star informed search method to optimize reaction wheels based on finite element analysis simulation results. The topology optimization algorithm is tested to evaluate its ability to eliminate checkerboard patterns and invalid geometries. Results show its capability to produce geometries that are structurally connected and free from zero-thickness, highlighting the potential of using global search-based optimization algorithms combined with finite element simulations for designing reaction wheels and other aerospace components.

Keywords: Topology Optimization, Multiphysics, Reaction Wheel

Nomenclature

V_{emf}	Back electromotive force
T	Torque
N_m	Number of magnets
N	Number of conductors per phase
B_g	Air gap flux density
L_{st}	Motor stack length
R_{ro}	Motor rotor outer radius
ω_m	Mechanical speed of motor
i, i_d, i_q	Current, Current d-axis, Current q-axis
K_e, K_t	Back electromotive force constant, Torque constant
$\lambda_{d,PM}$	Rotor permanent magnet d-axis flux linkage
L_d, L_q	Inductance d-axis, Inductance q-axis
$\boldsymbol{I}, \boldsymbol{\omega}$	Spacecraft inertia tensor, Spacecraft angular velocity
$\boldsymbol{G}_w, \boldsymbol{h}_w, I_w$	Reaction wheel torque, Reaction wheel angular momentum, Flywheel moment of inertia
$\boldsymbol{G_d}$	Disturbance torque
σ, τ	Normal and shear stress
ϵ, γ	Normal and shear strain
E, ν	Young's modulus, Poisson's ratio
$[K], [M]$	Stiffness matrix, Mass matrix

Acronyms/Abbreviations

BLDC	Brushless DC
FEA	Finite Element Analysis
ASC	A-Star Connectivity
NSGA-II	Non-dominated Sorting Genetic Algorithm II

1. Introduction

Reaction wheels play an important role in satellite control systems by enabling precise attitude control without expending fuel. A considerable amount of research has been dedicated to studying how reaction wheels can be used to fulfill the requirements of attitude determination and control systems. Zhang et al. [1] developed an intelligent wheel torque distribution algorithm to avoid reaction wheel disturbances such as stiction and resonance. Atallah et al. [2] used a set of three reaction wheels to satisfy attitude control requirements for AlainSat-1. Similarly, Alkatheeri et al. [3] used reaction wheels to simulate and validate sun pointing and nadir pointing operational modes for the GNSSaS6U CubeSat.

Significant efforts have been made to control multiple reaction wheels to meet the requirements of attitude determination and control systems; however, these approaches do not address the integration challenges associated with the large form factors of reaction wheels. Various types of reaction wheel designs have been proposed in the literature which have focused on the mechanical design, electromagnetic design, or electronic commutation method. Driedger et al. [4] designed a hard drive disk-based reaction wheel to achieve two-axis attitude control in a 3U CubeSat. Liu et al. [5] outlined the development of an ultralight radial flux brushless DC motor (BLDC) with a dual-layer rotor consisting of an integrated Halbach magnet array for a reaction wheel. Ratheesh et al. [6] used field-oriented control to reduce the torque ripple produced by a reaction wheel relative to traditional six-step commutation control algorithms. Other forms of reaction wheels also exist such as fluid-dynamic actuators which use mechanically pumped fluids [7], ferrofluid [8], or Galinstan [9].

Most reaction wheels use a BLDC motor paired with a flywheel to produce momentum and torque. These systems typically follow one of two primary designs: the first separates the brushless motor and flywheel, while the second integrates permanent magnets directly with the flywheel as shown in Figure 1. By merging the brushless motor rotor and flywheel into a unified component, reaction wheels can be designed with enhanced torque and momentum storage capacity per unit volume and mass.

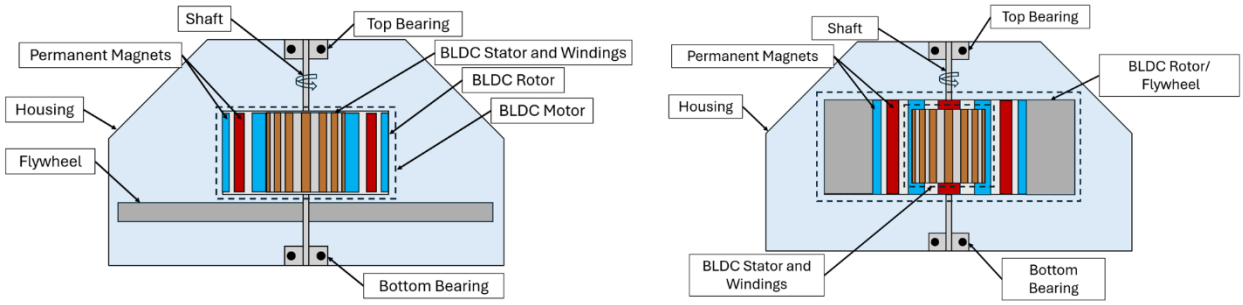

Figure 1 – Common reaction wheel configurations showing a design with a separate flywheel and motor (left) and an integrated flywheel and motor (right).

In contrast to the widely used BLDC motor-based reaction wheels, alternative electric motor types, such as the internal permanent magnet motor [10] and the permanent magnet assisted synchronous reluctance motor [11], have been used for electric vehicles. These motors integrate permanent magnets within the rotor structure, creating magnetic saliency. By carefully optimizing the design of the flux barriers and the shape of the magnets within the rotor, key performance metrics including average torque, torque ripple, and efficiency can be improved. Numerous researchers have explored using topology optimization to optimize motors with internal permanent magnets. Ishikawa et al. [12] optimized a permanent magnet synchronous motor rotor using a discrete variable based genetic algorithm. Sato et al. [13] performed topology optimization on an interior permanent magnet motor using a metaheuristic algorithm with normalized Gaussian networks.

A reaction wheel is an inherently electro-mechanical device, which relies on both electromagnetic and mechanical performance for efficient operation. For electric vehicles, research devoted to simultaneously improving the mechanical and electromagnetic performance has been performed via multiphysics topology optimization [14, 15]. Despite these efforts, there has been a lack of attention devoted to changing the basic architecture of reaction wheels using multiphysics-based optimization methods. The stringent mass and volume requirements of small satellites necessitates the need for smaller and lighter reaction wheels that can generate adequate torque and momentum while

minimizing torque disturbances. To fill this gap, this study introduces a multiphysics-driven topology optimization framework for reaction wheel devices, aiming to minimize the large form factors characteristic of the current modern designs. The algorithm we developed in this paper serves as the basis for high fidelity topology optimization that can accommodate multiphysics-based multi-objective functions compatible with finite element analysis (FEA) simulations. The main contributions of this paper are listed below:

- Creation of a multiphysics optimization workflow to enhance the performance of reaction wheels based on FEA simulation results.
- Development of a metaheuristic-based topology optimization algorithm that can produce structurally connected geometries without zero thickness regions.
- Development of the A-Star Connectivity (ASC) algorithm to implement connectivity-based constraints for topology optimization processes.

The structure of this paper is as follows: Section 2 explains the theory behind reaction wheel design using multiphysics-based optimization methods. Section 3 provides an in-depth summary of the algorithm we developed to support multiphysics-based topology optimization. Section 4 outlines and discusses the findings from the simulations conducted using the developed algorithm. Finally, Section 5 summarizes the importance of the results, highlights their limitations, and provides directions for future work.

2. Theory and Formulation

This section presents the fundamental equations related to the electromagnetic and structural design of a reaction wheel. Section 2.1 presents theory related to the electromagnetic design of reaction wheels, while Section 2.2 presents the theory related to the mechanical design of reaction wheels.

2.1 Electromagnetic Design Theory

All three-phases of a permanent magnet synchronous motor contribute to the overall torque produced by a reaction wheel. The per-phase electromagnetic torque, T, and back electromotive force, V_{emf}, produced by a brushless surface mounted permanent magnet motor can be expressed with the following equations [16]:

$$V_{emf} = 2N_m N B_g L_{st} R_{ro} \omega_m = K_e \omega_m \tag{1}$$

$$T = \frac{V_{emf} i}{\omega_m} = 2N_m N B_g L_{st} R_{ro} i = K_t i \tag{2}$$

$$K_e = K_t \tag{3}$$

Where:

- N_m: Number of magnets
- N: Number of conductors per phase
- B_g: Air gap flux density
- L_{st}: Stator stack length
- R_{ro}: Rotor outer radius
- ω_m: Motor mechanical speed
- i: Phase current
- K_e: Back electromotive force constant
- K_t: Torque constant

The power balance considering all three-phases for any arbitrary back electromotive force and current waveforms can be expressed as:

$$T \cdot \omega_m = V_{emf,a} i_a + V_{emf,b} i_b + V_{emf,c} i_c \tag{4}$$

The total output torque of the reaction wheel motor varies depending on the commutation method. Using sinusoidal currents to drive the reaction wheel the total ideal torque is [17]:

$$T = \frac{3}{2} K_t i \tag{5}$$

Conversely, the total torque produced using six-step commutation to drive the reaction wheel is [17]:

$$T = 2K_t i \tag{6}$$

Traditionally, brushless surface-mounted permanent magnet motors have been used in reaction wheel designs. Since these motors have uniform reluctance across all flux paths, they are non-salient. As a result, they generate negligible reluctance torque, which is the torque produced due to a ferromagnetic rotors tendency to align itself with the stator's generated magnetic field. The general equation for the torque produced by an internal permanent magnet motor, which accounts for both permanent magnet and reluctance torques is [18]:

$$T = \frac{1}{4} N N_m (\lambda_{d,PM} i_q + (L_d - L_q) i_d i_q) \tag{7}$$

Where:

- $\lambda_{d,PM}$: Rotor permanent magnet d-axis flux linkage
- L_d: Inductance d-axis
- L_q: Inductance q-axis
- i_d: Current d-axis
- i_q: Current q-axis

The rotor topology governs the difference between d-axis (direct axis, reference rotor magnetic field axis) and q-axis (quadrature axis, orthogonal to and leading the d-axis) inductances, directly influencing the total output torque. Optimizing this topology can increase the reluctance torque; however, increasing torque often comes at the cost of higher torque ripple [12, 13]. To achieve the optimal balance between maximizing torque and minimizing torque ripple, multi-objective optimization methods are required to find rotor topologies consisting of both ferromagnetic and permanent magnetic materials.

The equations outlined above are idealized representations that illustrate the relationship between the rotor's topology and performance metrics like output torque and back electromotive force. However, electric machine design is complex and simplified analytical equations cannot be used to design an actual motor to sufficiently high degrees of accuracy [16]. To obtain high fidelity results for an electric machine's speed, torque, and torque ripple performance FEA is required.

2.2 Structural Design Theory

Reaction wheels generate torque and store momentum which can be used to control a spacecraft's attitude according to Euler's equation:

$$\boldsymbol{I\dot{\omega}} + \boldsymbol{G}_w + \boldsymbol{\omega}^{\times}(\boldsymbol{I\omega} + \boldsymbol{h}_w) = \boldsymbol{G}_d \tag{8}$$

Where:

- $\boldsymbol{I}$: Spacecraft inertia tensor
- $\boldsymbol{\omega}$: Spacecraft angular velocity
- $\boldsymbol{h}_w$: Reaction wheel angular momentum
- $\boldsymbol{G}_w$: Reaction wheel torque
- $\boldsymbol{G}_d$: Disturbance torque

Ensuring that a reaction wheel has adequate momentum storage allows for enhanced slewing capabilities and improved three-axis stability in satellites. The energy density of a flywheel represents the amount of momentum or energy it can safely store relative to its mass [19]. Energy density of a flywheel can be expressed using the following equation [19]:

$$e = \frac{1}{m} \cdot \frac{1}{2} I_w \omega_m^2 \tag{9}$$

Where:

- I_w : Flywheel moment of inertia
- m: Flywheel mass
- ω_m: Angular velocity of the flywheel

As a rotor rotates it experiences an apparent radial force due to a non-inertial (rotating) reference frame, commonly referred to as a "centrifugal force", which is expressed as:

$$F = mr\omega_m^2 \tag{10}$$

Stresses induced from centrifugal forces primarily act in the radial and tangential direction of a rotating disk. The stress distribution in the axial direction can be neglected and the problem can be simplified to a 2D plane stress problem. For a plane stress problem, the relationship between stress and strain can be expressed as follows:

$$\begin{pmatrix} \sigma_x \\ \sigma_y \\ \tau_{xy} \end{pmatrix} = \frac{E}{1-\nu^2} \begin{pmatrix} 1 & \nu & 0 \\ \nu & 1 & 0 \\ 0 & 0 & (1-\nu)/2 \end{pmatrix} \begin{pmatrix} \epsilon_x \\ \epsilon_y \\ \gamma_{xy} \end{pmatrix} \tag{11}$$

The von-Mises yield criterion can be used to predict when the reaction wheel rotor is expected to yield under centrifugal loading conditions. According to the von-Mises yield stress criterion, for a 2D plane stress problem, if the von-Mises stress σ_v exceeds the yield stress of the material σ_y the rotor will yield:

$$\sigma_v = \sqrt{\sigma_{11}^2 + \sigma_{22}^2 - \sigma_{11}\sigma_{22} + 3\sigma_{12}^2} \geq \sigma_y \tag{12}$$

Where the stress components in Equation 11 are along the coordinate axis and the stress components in Equation 12 are along the principal axis. In addition to plastic deformation, the flywheel's first natural frequency should be maximized and be greater than the launch vehicle and nominal operation wheel speed frequencies. Natural frequencies can be computed by solving the following eigenvalue problem numerically:

$$([K] - \omega_i^2[M])\{\phi_i\} = \{0\} \tag{13}$$

When optimizing the rotor topology as outlined in Section 2.1, thin structural members may form, which can reduce the rotor's structural integrity. Due to the complexity of the generated rotor topologies, FEA is required to accurately determine the state of stress and natural frequencies of the rotor.

3. Optimization Process

This section presents the development of a topology optimization framework which can support coupled electromagnetic and structural topology optimization. The optimization problem involves maximizing torque, momentum storage, and rotor natural frequencies, while minimizing both mass and torque ripple. Section 3.1 describes the overall optimization workflow. Section 3.2 provides an overview of the use of the ASC algorithm.

3.1 General Multiphysics Optimization Workflow

Figure 2 shows the overall reaction wheel multiphysics topology optimization workflow. The algorithm's first phase initializes the design space, discretizes the rotor geometry into a finite element mesh consisting of triangular elements, and defines elements that are within the design space. Once this is complete, the optimization problem can be mathematically defined as:

$$\begin{array}{lccl} \text{Minimize:} & f_m(\boldsymbol{x}) & & m = 1,2,\dots,M \\ \text{Subject to:} & g_j(\boldsymbol{x}) \leq 0 & & j = 1,2,\dots,J \\ & \boldsymbol{x}_p = (x_1, x_2, x_3, \dots, x_N)^T, & x_i \in \{0,1,2\} & p = 1,2,\dots,P \\ & & & i = 1,2,\dots,N \end{array} \tag{14}$$

Where M is the number of objective functions, J is the number of constraints, P is the population size, and N is the number of design variables in the problem. The proposed topology optimization approach discretizes the reaction wheel rotor into N finite elements, each of which can exist in one of three states: 1, indicating the presence of ferromagnetic material; 2, indicating the presence of permanent magnetic material; or 0, representing the absence of all material. A multi-objective optimization algorithm can then be used to determine the Pareto optimal solutions $\boldsymbol{x}_i^*$ that yield the best trade-off between the competing objective functions. To simultaneously optimize the reaction wheel's structural and electromagnetic characteristics the following five objectives are proposed:

- $f_1(\boldsymbol{x}) = -T_{\text{avg}}(\boldsymbol{x})$: Average Electromagnetic Torque
- $f_2(\boldsymbol{x}) = \ T_{ripple}(\boldsymbol{x})$: Torque Ripple
- $f_3(\boldsymbol{x}) = -F_{n1}(\boldsymbol{x})$: First Natural Frequency of the Rotor
- $f_4(\boldsymbol{x}) = \ m(\boldsymbol{x})$: Rotor Mass
- $f_5(\boldsymbol{x}) = -I(\boldsymbol{x})$: Rotor Moment of Inertia

The average electromagnetic torque $T_{avg}(\boldsymbol{x})$ is obtained through FEA simulations. Similarly, the torque ripple $T_{ripple}(\boldsymbol{x})$ can be calculated by taking the difference between the maximum and minimum torque and dividing by the average torque $T_{avg}(\boldsymbol{x})$:

$$T_{ripple}(\boldsymbol{x}) = \frac{T_{max}(\boldsymbol{x}) - T_{min}(\boldsymbol{x})}{T_{avg}(\boldsymbol{x})} \tag{15}$$

The first natural frequency of the rotor $F_{n1}(\boldsymbol{x})$ can be computed from Equation (13). The rotor moment of inertia and mass are physical properties that can be computed using the following equations:

$$I(\boldsymbol{x}) = \sum_{i=1}^{n} m_i r_i^2 \tag{16}$$

$$m(\boldsymbol{x}) = \sum_{i=1}^{n} m_i \tag{17}$$

Constraints are used to classify solutions as valid or invalid in the optimization process. This optimization workflow includes the following constraints:

- $g_1(\boldsymbol{x}) = \ \sigma_c(\boldsymbol{x})$: Maximum Stress Constraint
- $g_2(\boldsymbol{x}) = \ g_2(A^*(\boldsymbol{x}))$: Structural Connectivity Constraint
- $g_3(\boldsymbol{x}) = \ g_3(t(\boldsymbol{x}))$: Zero Thickness Constraint

The maximum stress constraint $\sigma_c(\boldsymbol{x})$ relates the maximum computed von-Mises stress from FEA simulations and compares it to the yield stress of the constitutive material of the rotor considering a defined factor of safety (FS). Once the state of stress is computed using FEA, the maximum stress constraint can be used to penalize and constrain the solutions generated by the optimization algorithm:

$$\sigma_c(\boldsymbol{x}) = \begin{cases} 1, & \zeta > 1 \\ -1, & \zeta \leq \dfrac{1}{\text{FS}} \\ \dfrac{\zeta - 1/\text{FS}}{1 - 1/\text{FS}}, & \text{otherwise} \end{cases} \tag{18}$$

$$\zeta = \frac{\max\left(\sigma_v(\boldsymbol{x})\right)}{\sigma_y} \tag{19}$$

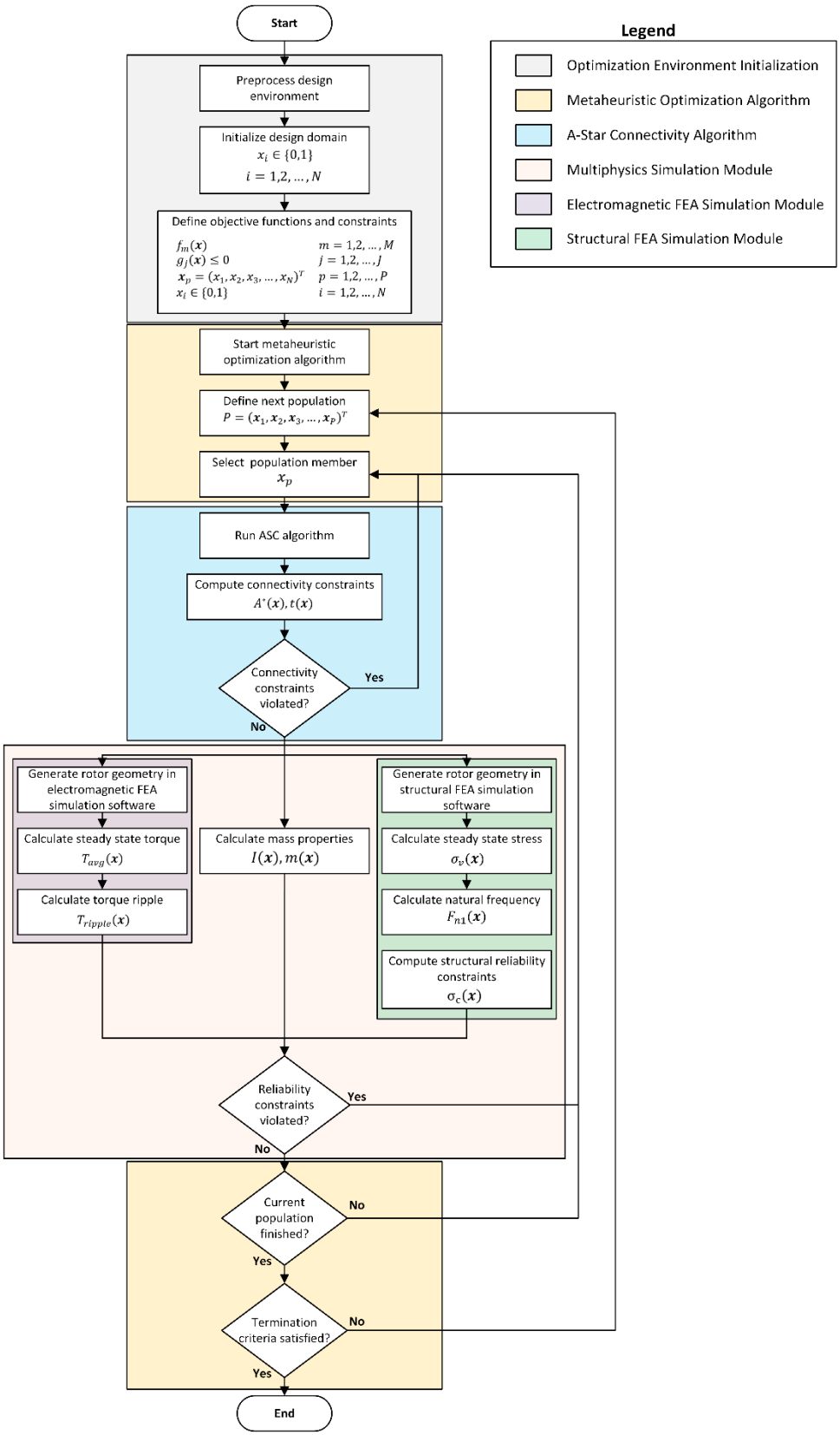

Figure 2 – Reaction wheel multiphysics topology optimization workflow.

Constraints $g_2(\boldsymbol{x})$ and $g_3(\boldsymbol{x})$ are based on structural connectivity. Certain values for $\boldsymbol{x}_p$ may produce material distributions that are structurally disconnected or have a high degree of checkerboarding resulting in regions of zero thickness. Thus, it is important to be able to constrain the optimization algorithm so it can learn how to produce connected structures. Determining if a structure is disconnected or has zero thickness is done computationally and is discussed in Section 3.2. The general mathematical description of $A^*(\boldsymbol{x})$ and $t(\boldsymbol{x})$ are using the following equations:

$$A^*(\boldsymbol{x}) = \begin{cases} 1, & \text{structurally disconnected} \\ -1, & \text{structurally connected} \end{cases} \tag{20}$$

$$t(\boldsymbol{x}) = \begin{cases} \beta, & \text{zero thickness detected} \\ -1, & \text{no zero thickness detected} \end{cases} \tag{21}$$

Where β is the ratio of elements producing zero thickness to the total number of elements in the design space.

The convergence criteria in the overall workflow shown in Figure 2 is governed by a user defined total number of iterations or the relative change in the objective function between successive iterations.

3.2 A-Star Connectivity Algorithm for Topology Optimization

The A-Star Connectivity (ASC) algorithm introduced in this work adapts A-Star informed search algorithms, originally designed for robotic path planning [20], to address and eliminate the "checkerboard" patterns often observed in topology optimization from prior research in the literature [12, 13]. Figure 3 graphically shows how the ASC algorithm works to allow metaheuristic optimization algorithms to produce structures that are connected and valid.

A-Star is a node traversal algorithm. In this research a node n is defined as the centroid of an individual element (design variable). Once preserved regions and the design vector are defined, the first step of ASC is to determine if a valid path exists between each of the preserved regions. If a path exists, the structure is classified as globally connected, otherwise it is classified as globally disconnected. ASC confirms the existence of a path and optimally finds this path by minimizing the following equation [20]:

$$f(n) = g(n) + h(n) \tag{22}$$

Where:

- $f(n)$: F-Score (ASC cost function)
- $g(n)$: G-Score (known cost to travel to a valid neighbouring element)
- $\mathrm{h}(n)$ H-Score (heuristic cost to travel from a neighbouring element to the target)

The heuristic score $\mathrm{h}(n)$ is used to prioritize the exploration of potential paths. The ASC algorithm we developed uses the Euclidean distance:

$$h(n) = \sqrt{\left(x_{target} - x_n\right)^2 - \left(y_{target} - y_n\right)^2} \tag{23}$$

During topology optimization, regions can exist which produce zero thickness. This occurs when two voided elements join at a node without any other voided elements connecting them. This will cause the part to have an infinite stress concentration and will also be impossible to manufacture. This research implements the following two checks to ensure that zero thickness will not occur in the optimized parts:

- Check #1: Ensure that any voided element sharing a vertex with another voided element also shares a neighbouring element that is voided.
- Check #2: Ensure that all edge elements with a vertex on the boundary of the geometry (green elements in Figure 3b) have at least one neighboring edge element that is also voided.

These checks can overestimate the actual number of voided elements that produce zero thickness. This overestimation arises because, with triangular mesh elements, two voided elements connected at a vertex can be joined by multiple neighboring void edge elements. This is later discussed in Section 4.

Referring to Figure 3, Part (a) shows two distinct preserved regions (blue), one region near the shaft location and the other region at the outer edge of the rotor. All other elements are a part of $\boldsymbol{x}_p$ with the black elements being void and grey elements being solid. Part (b) shows how edge elements are classified. Part (c) shows global connectivity of the rotor. The optimal path is shown using the purple line with voids shown as red circles. Part (d) shows regions that are connected (green) and disconnected (red). During the optimization process any disconnected elements are removed from the geometry before FEA simulations are conducted. This process is acceptable since the process of determining connectivity is deterministic and does not affect the metaheuristic algorithm. Part (e) shows the voided elements that are producing zero thickness according to the checks above. Part (f) shows how the rotor from the quarter scale model is reflected to produce an entire rotor geometry.

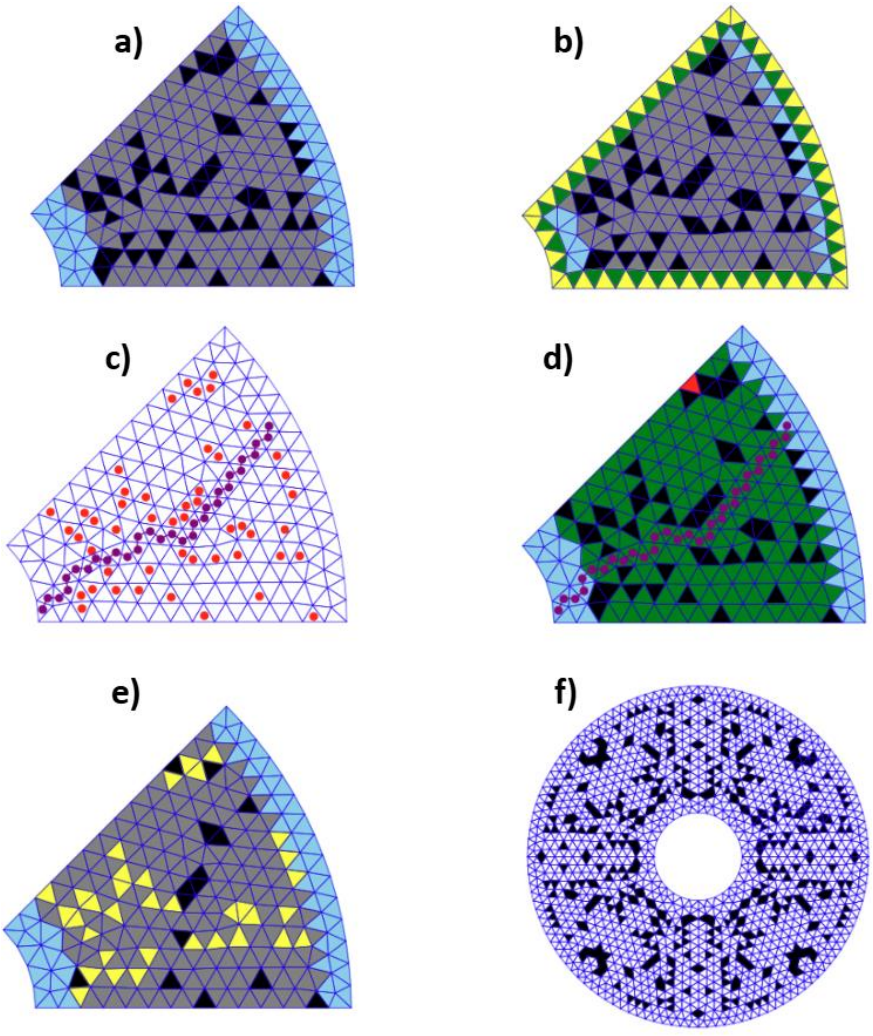

Figure 3 – The ASC algorithm graphical flow diagram. Part (a) shows an example candidate solution with preserved regions (blue), solid elements (grey, 1), and void elements (black, 0). Part (b) shows how edges are identified. Part (c) shows the optimal path (purple) between each preserved region in the presence of voids (red). Part (d) shows connected (green) and disconnected (red) elements after running the ASC algorithm. Part (e) shows classified elements (yellow) which contribute to zero thickness. Note some elements are not causing zero thickness due to limitations discussed previously. Part (f) shows the full rotor generated from the sectioned model using mirroring.

4. Results and Discussion

This section presents the preliminary simulation results from the implementation of the algorithm outlined in Section 3. The scope of the optimization algorithm involves evaluating the optimization algorithm's ability to eliminate structural connectivity requirements, $g_2(\boldsymbol{x})$, and zero-thickness constraint violations, $g_3(\boldsymbol{x})$, while simultaneously minimizing mass and maximizing rotor moment of inertia. FEA simulations are not performed, as the focus is solely on assessing the algorithm's ability to handle the aforementioned constraints. Section 4.1 summarizes the simulation and optimization parameters used. Section 4.2 provides a summary of the simulation results and a discussion of their implications.

4.1 Optimization Scope and Simulation Parameters

Table 1 provides a summary of the simulation parameters used in the optimization scenario. Each variable in population member $\boldsymbol{x}_p$ is constrained to be 0 or 1. A 45-degree angle of symmetry was chosen for simplicity to define the rotor geometry. For reaction wheel rotors incorporating embedded magnets, the angle of symmetry can be determined by the number of poles and windings per phase when conducting full-scale multiphysics simulations.

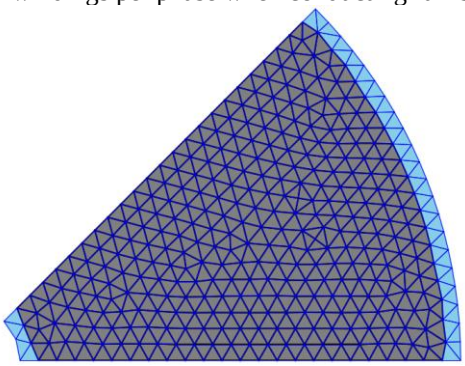

Figure 4 – Initialized design environment with preserved regions (blue) and the design space (grey). The depicted rotor is reflected about the axis of rotation every 45 degrees to create the full rotor geometry.

Table 1 summarizes the information related to the metaheuristic optimization method. Non-dominated Sorting Genetic Algorithm II (NSGA-II), as implemented in "pymoo" [21], was used as the metaheuristic for the algorithm outlined in Section 3. NSGA-II was selected due to its capability of handling multi-objective optimization problems in binary design spaces [21, 22]. The default two-point crossover operator was chosen for the crossover method, while the default bit-flip operator was utilized for mutation [21]. Both crossover and mutation rates were set to values similar to those reported previously in the literature [22]. Each population member is comprised of 605 binary variables, as illustrated in Figure 4. Binary random sampling was used to initialize the first population, with a 70% probability assigned to binary variables being 1 (solid). A total of 30,000 simulations were performed using a population size of 100 individuals, with termination criteria set to a maximum of 300 generations. The number of total simulations was selected on the basis of available computational resources.

Table 1 – Simulation parameters related to the reaction wheel rotor and operational environment.

Simulation Parameter	**Value**
Rotor Outer Diameter	270 mm
Rotor Inner Diameter	30 mm
Symmetry Angle	45 degrees
Optimization Parameter	**Specification**
Algorithm	NSGA-II [21]
Crossover Method	Standard Four-Point Crossover [21]
Mutation Method	Standard Bit Flip Mutation [21]
Population Size	100
Number of Generations	300
Number of Variables	605

4.2 Optimization Results

Figure 5 illustrates the convergence history of the optimization algorithm. During the first three generations, high average constraint violation values indicate widespread violations of the two constraints: connectivity and zero thickness. As the optimization progresses, both the average and minimum constraint violation values steadily decrease, approaching 0. By the 57th generation, the minimum constraint violation reaches zero, signifying that the algorithm has successfully generated rotor topologies that satisfy structural connectivity and zero thickness constraints. This phase of the convergence plot, driven by the ASC algorithm, is referred to as the "connectivity learning zone." Within six additional generations, the average constraint violation also drops to zero. The results suggest that the developed ASC algorithm can effectively eliminate checkerboard patterns prevalent in previously reported topology optimization algorithms for structural and electromagnetic design problems. The results in Figure 5 shows that after the initial connectivity learning zone, there is a low number of constraint violations suggesting that other global minima locations could be unexplored due to a lack of exploration later in the optimization process. Future work should also be dedicated to using other metaheuristic algorithms which use more exploration later in the optimization process.

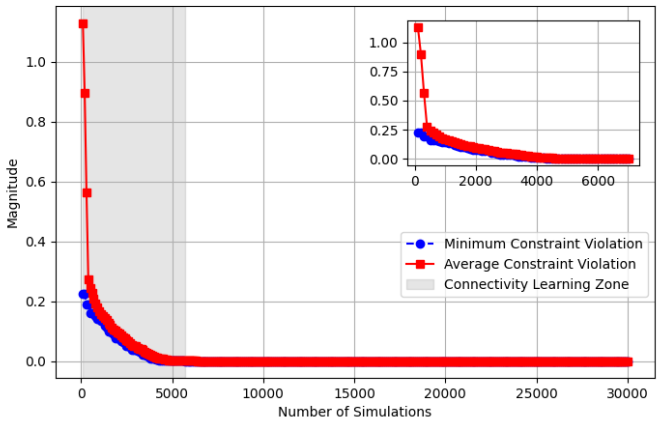

Figure 5 – Optimization convergence history. Combined with the ASC algorithm, the implemented version of NSGA-II took approximately 5700 simulations to learn how to produce structurally connected parts with no zero-thickness geometry.

5. Conclusions and Future Research Directions

This study presents a multiphysics-based topology optimization framework that can be used to design reaction wheels with enhanced mechanical and electromagnetic performance. We developed a modular optimization algorithm that uses the ASC algorithm in combination with NSGA-II to facilitate metaheuristic-based topology optimization with FEA-based objectives. We assessed the algorithm's performance using a test scenario to determine its ability to eliminate structural connectivity and zero-thickness constraint violations. Results show that the topology optimization algorithm is able to produce structurally connected structures with no zero thickness regions. These results open new possibilities for leveraging global search-based optimization algorithms in conjunction with commercial FEA simulation software for custom multiphysics-driven topology optimization problems. Currently the zero thickness detection rules are more stringent than necessary. Future work will focus on enhancing the ASC algorithm to identify zero-thickness geometries and incorporate additive manufacturing constraints. Additionally, integrating artificial intelligence could accelerate the detection of structural connectivity and zero-thickness regions. Further research will also explore full-scale electromagnetic and structural topology optimization, incorporating torque and resonance frequency-based objective functions.

References

[1] T. Zhang and P. Ferguson, "Optimal Reaction Wheel Control with Stiction and Resonance Avoidance," in *Springer Aerospace Technology*, 2022. doi: 10.1007/978-3-030-94628-9_30.

[2] M. Atallah, S. Jamali, M. Okasha, and A.-H. Jallad, "Analysis and Simulation of Attitude Determination and Control Subsystem of a 3U CubeSat: AlainSat-1," in *17th International Conference on Space Operations*, Dubai, United Arab Emirates, Mar. 2023.

[3] A. Alkatheeri, M. Okasha, H. Elshimy, and T. N. Dief, "Design and Implementation of Attitude Control System for GNSSaS6U CubeSat Satellite," in *17th International Conference on Space Operations*, Dubai, United Arab Emirates, Mar. 2023.

[4] M. Driedger, J. Chornick, E. Olaniyanu, K. Dick, R. Sahani, and P. Ferguson, "Using hard drive based reaction wheels for attitude control on the TSAT-5 CubeSat," in *Proceedings of the International Astronautical Congress, IAC*, 2019.

[5] N. W. Liu, K. Y. Hung, B. T. Lyu, and S. C. Yang, "Ultra-Light Reaction Wheel with Dual-layer rotor and Single-side Halbach Magnet Array for CubeSat," in *2023 IEEE Energy Conversion Congress and Exposition, ECCE 2023*, 2023. doi: 10.1109/ECCE53617.2023.10362039.

[6] K. Ratheesh, S. Sreejith, and T. R. Haridas, "Field-Oriented Control for Performance Improvement in Reaction Wheels and Implementation of Algorithm in FPGA," in *Lecture Notes in Mechanical Engineering*, 2023. doi: 10.1007/978-981-19-7474-8_13.

[7] S. Akbaritabar, R. Esmaelzadeh, and R. Zardashti, "Design of attitude control servomechanisms with fluid ring and CMG for rigid satellite," *Journal of Aerospace Technology and Management*, vol. 10, 2018, doi: 10.5028/jatm.v10.950.

[8] Ehresmann, M., Zajonz, S., Korn, C. et al. Ferrofluid reaction wheel development and in-orbit verification. CEAS Space J (2025). https://doi.org/10.1007/s12567-025-00601-2.

[9] D. Noack and K. Brieß, "Laboratory investigation of a fluid-dynamic actuator designed for CubeSats," *Acta Astronaut*, vol. 96, no. 1, 2014, doi: 10.1016/j.actaastro.2013.11.030.

[10] H. S. Seol, J. Lim, D. W. Kang, J. S. Park, and J. Lee, "Optimal Design Strategy for Improved Operation of IPM BLDC Motors with Low-Resolution Hall Sensors," *IEEE Transactions on Industrial Electronics*, vol. 64, no. 12, 2017, doi: 10.1109/TIE.2017.2716908.

[11] Y. Kong, M. Lin, M. Yin, and L. Hao, "Rotor structure on reducing demagnetization of magnet and torque ripple in a PMa-synRM with ferrite permanent magnet," *IEEE Trans Magn*, vol. 54, no. 11, 2018, doi: 10.1109/TMAG.2018.2827104.

[12] T. Ishikawa, K. Nakayama, N. Kurita, and F. P. Dawson, "Optimization of rotor topology in PM synchronous motors by genetic algorithm considering cluster of materials and cleaning procedure," *IEEE Trans Magn*, vol. 50, no. 2, 2014, doi: 10.1109/TMAG.2013.2282365.

[13] T. Sato, K. Watanabe, and H. Igarashi, "Multimaterial topology optimization of electric machines based on normalized Gaussian network," *IEEE Trans Magn*, vol. 51, no. 3, 2015, doi: 10.1109/TMAG.2014.2359972.

[14] W. Wu, Q. Chen, X. Zhu, F. Zhao, and Z. Xiang, "Electromagnetic-mechanical coupling optimization of an IPM synchronous machine with multi flux barriers," *Energies (Basel)*, vol. 13, no. 7, 2020, doi: 10.3390/en13071819.

[15] Y. Li, B. Ma, J. Zheng, J. Zhu, and G. Lei, "Electromagnetic and Mechanical Topology Optimization for SynRM Rotors Considering High Dimensional Constraints," *IEEE Transactions on Industrial Electronics*, vol. 70, no. 12, 2023, doi: 10.1109/TIE.2023.3234146.

[16] D. Hanselman, *Brushless Permanent Magnet Motor Design*, 2nd ed. Magna Physics Publishing, 2006.

[17] J. R. Mevey, "Sensorless Field Oriented Control of Brushless Permanent Magent Synchronous Motors," 2006.

[18] S. T. Lee and L. M. Tolbert, "Analytical method of torque calculation for interior permanent magnet synchronous machines," in *2009 IEEE Energy Conversion Congress and Exposition, ECCE 2009*, 2009. doi: 10.1109/ECCE.2009.5316263.

[19] L. Jiang and C. W. Wu, "Topology optimization of energy storage flywheel," *Structural and Multidisciplinary Optimization*, vol. 55, no. 5, 2017, doi: 10.1007/s00158-016-1576-1.

[20] G. Tang, C. Tang, C. Claramunt, X. Hu, and P. Zhou, "Geometric A-Star Algorithm: An Improved A-Star Algorithm for AGV Path Planning in a Port Environment," *IEEE Access*, vol. 9, 2021, doi: 10.1109/ACCESS.2021.3070054.

[21] J. Blank and K. Deb, "Pymoo: Multi-Objective Optimization in Python," *IEEE Access*, vol. 8, 2020, doi: 10.1109/ACCESS.2020.2990567

[22] T. Kunakote and S. Bureerat, "Multi-objective topology optimization using evolutionary algorithms," *Engineering Optimization*, vol. 43, no. 5, 2011, doi: 10.1080/0305215X.2010.502935.